Computer Simulation of Isothermal Fluidization in Large-scale Laboratory Rigs

D. W. Richner
Mechanical Engineering Department
University of Massachusetts
Amherst, MA 01003

T. Minoura
Mechanical Engineering Research Laboratory
Kobe Steel Ltd.
Kobe, Japan

J. W. Pritchett
S-Cubed
La Jolla, CA 92037

T. R. Blake
Mechanical Engineering Department
University of Massachusetts
Amherst, MA 01003

Finite-difference computer models have been used by several investigators to predict hydrodynamic mixing in fluidized beds. In the present study the finite-difference model CHEMFLUB is used to simulate cold, isothermal mixing in axisymmetric fluidized beds. The bed geometries and the operating conditions are based upon those of two large-scale laboratory cold flow rigs. The finite-difference model is an iterative, implicit formulation to solve continuum equations describing the gas and particle dynamics of fluidization. Comparisons with experimental data are presented. It is shown that the model provides a good prediction of jet penetration height, bubble frequency, and bubble velocity.

Introduction

The complexities associated with mixing in fluidized beds are often studied with models describing fluid and particle dynamics in the bed. Since there are a variety of such models it is convenient to catalog them as either classical models, dimensional analysis and scaling, or hydrodynamic models. These models have respective strengths and weaknesses.

Classical models are described by Davidson and Harrison (1963), Kunii and Levenspiel (1969), and Yates (1983). Such models are based on the two-phase theory of fluidization. Typically, one phase is a particulate emulsion phase, in the state of minimum fluidization, and the second is a bubble phase (Davidson and Harrison, 1963). These models permit the prediction of complex chemistry, however the hydrodynamic mixing is not predicted. Rather, the details of the flow, such as frequency, size, and shape of the bubbles, are specified a priori in order to calculate the coupling of the hydrodynamics to the chemistry.

Dimensional analysis and scaling has been widely used to correlate and scale hydrodynamic phenomena of fluidization. Recently, Fitzgerald and Glicksman (1983), Glicksman (1984, 1988), and Blake et al. (1989) have suggested that such correlations should be based on universal sets of nondimensional hydrodynamic parameters. Since such nondimensional parameters are fewer in number than the total number of physical variables, the correlation and experimentation are often simplified.

Hydrodynamic models are described by Blake and Chen (1981), Schneyer et al. (1981), Gidaspow et al. (1981), Chan et al. (1982), and Gidaspow (1986). These models are based upon a continuum multiphase formulation of gas and particle dynamics. The formulation is expressed as a system of partial differential equations, which are solved through finite-difference techniques. The hydrodynamic models differ from classical models in that they provide predictions of the hydrodynamic mixing in fluidized beds. Time histories and spatial distributions of the important process variables are explicitly predicted; for example, the development and rise of bubbles evolve naturally from the numerical calculation of the hydrodynamics within the reactor. Of course, these hydrodynamic predictions are sensitive to the particle-particle and particle-gas forces. The description of such forces is a major uncertainty and is a subject of continuing research.

For the present study, CHEMFLUB, the hydrodynamic model of Schneyer et al. (1981), is used to predict fluidization in two cold flow laboratory rigs, the Westinghouse agglomerating combustor/gasifier (Yang and Keairns, 1978) and the KRW agglomerating combustor/gasifier (Yang et al., 1984). Also,

specific and limited parametric studies are used to analyze the influences of reactor walls and injected gas flow distribution on the bubble formation. In order to facilitate the simulation of the experimental reactors, modifications are made to the CHEMFLUB model. These modifications are justified by the physics of the governing equations and the formulation of the numerical algorithms.

The predictions from CHEMFLUB are consistent with earlier results of Blake and Chen (1981) for the Westinghouse rig, and are in agreement with the experimental observations of Yang and Keairns (1978). Further, when the model is applied to the KRW rig, a good comparison between the calculations and many aspects of the experimental observations of Yang et al. (1984) are demonstrated. However, some differences between calculation and experiment are observed.

Theoretical Basis for CHEMFLUB

The gas and particle dynamics of fluidization may be defined by conservation equations of mass and momentum for the gas and solid phases. For the present study, certain restrictions and assumptions are placed on these equations: fluidization is restricted to an isothermal environment, and particles are assumed to be monosize and rigid, but nonspherical. The theoretical formulation of Anderson and Jackson (1967) is used by Pritchett et al. (1978) to derive the continuum multiphase conservation equations and provide the basis for CHEMFLUB. The numerous assumptions and the specification of the physicochemical properties of the gas and solid phases are discussed by Pritchett et al. while the salient features of the numerical formulation in CHEMFLUB are summarized by Chen (1981). For the present study these equations are merely stated in Cartesian tensor notation:

Conservation of gas phase mass

$$\frac{\partial}{\partial t}(1-\theta)\rho + \frac{\partial}{\partial x_i}(1-\theta)\rho v_i = 0 \tag{1}$$

Conservation of solid phase mass

$$\frac{\partial}{\partial t}\theta\rho^s + \frac{\partial}{\partial x_i}\theta\rho^s u_i = 0 \tag{2}$$

Conservation of gas phase momentum

$$-\frac{\partial}{\partial x_i}p - \frac{B\{v_i - u_i\}}{1-\theta} = 0 \tag{3}$$

Conservation of solid phase momentum

$$\frac{\partial}{\partial t}\theta\rho^s u_i + \frac{\partial}{\partial x_j}\theta\rho^s u_i u_j = \frac{\partial}{\partial x_j}\tau_{ij} + \theta\rho^s g_i - \frac{\partial}{\partial x_i}(1-\theta)p \tag{4}$$

where, $\rho(\rho^s)$ is the gas (solid) density, v_i (u_i) is the gas (solid) velocity, and θ is the solid volume fraction. The gas stress tensor is represented by $-\delta_{ij}p$, while τ_{ij} represents the solid stress tensor. B is the drag coefficient, which is a function of the solid volume fraction and the local Reynolds number. Pritchett et al. and the present study assume that the solid phase stress tensor τ_{ij} is Newtonian and contains both hydrostatic and deviatoric terms:

$$\tau_{ij} = \delta_{ij}\left[-(p^s + \theta p) + \lambda^s\left(\frac{\partial}{\partial x_k}u_k\right)\right] + \mu^s\left(\frac{\partial}{\partial x_j}u_i + \frac{\partial}{\partial x_i}u_j - \frac{2}{3}\delta_{ij}\frac{\partial}{\partial x_k}u_k\right) \tag{5}$$

The constitutive equations and interaction functions in Eqs. 1–5 are developed from experimental data. Specifically, Pritchett et al. (1978) and Chen (1981) provide descriptions of: $p^s(\theta)$, the normal component of particle-particle interactions; λ^s, the bulk viscosity of particle assemblage; μ^s, the shear viscosity of particle assemblage; and B, the particle-gas drag coefficient. For example, the particle-gas drag coefficient is derived from data on pressure drop at minimum fluidization (the previous conservation equations are rewritten for minimum fluidization and are fitted to the data). The drag coefficient can be expressed in terms of K, the permeability of the fluidized bed:

$$B = \frac{(1-\theta)^2\mu}{K}$$

In Chen (1981) K is expressed as a product of functions involving θ and a local "Reynolds number," N:

$$K = \frac{F_1(\theta)F_2(N)}{\tilde{A}^2}; \quad N = \frac{(1-\theta)\rho v}{\tilde{A}\mu}$$

$\tilde{A}$ is the specific surface of the solid particles, where $\tilde{A}$ is related to the particle shape factor ϕ_s and the particle diameter d: $\tilde{A} = 6/d\phi_s$. The functions F_1 and F_2 are established by laboratory data.

In the present study the shape factor is incorporated into the CHEMFLUB model. The specific changes were implemented in subroutine PERMFN, in which the permeability K is calculated during the computational cycle (Chen, 1981). In addition, the present version of CHEMFLUB differs from that described by Schneyer et al. and Chen in that the subroutines UXVIS1, VISFRC, and QFIND have been altered. (The new subroutines are described in the supplementary material.)

Axisymmetric Models of the Westinghouse and KRW Cold Flow Rigs

The CHEMFLUB numerical calculations are based on the physical environments of the Westinghouse 30 cm dia. (Yang and Keairns, 1978) and KRW 300 cm dia. (Yang et al., 1984) cold flow rigs. The dimensions, flow distributions, gas and solid properties, and other characteristics of these reactors serve as initial and boundary conditions for the CHEMFLUB model.

Figure 1 shows the Westinghouse cold flow semicircular rig, which represents, in a scaled fashion, the geometry of the Westinghouse combustor/gasifier. To allow visual observation of experiments, this semicircular column is constructed from Plexiglas. The total height of the rig is 560 cm. The gasifier section of the column has an internal diameter of 28.6 cm and a height of 305 cm.

Bed material used in the Westinghouse experiment consists of hollow epoxy spheres ranging from 1.78 to 3.81 mm dia. Yang and Keairns (1978) report a weighted diameter of 2,800 μm.

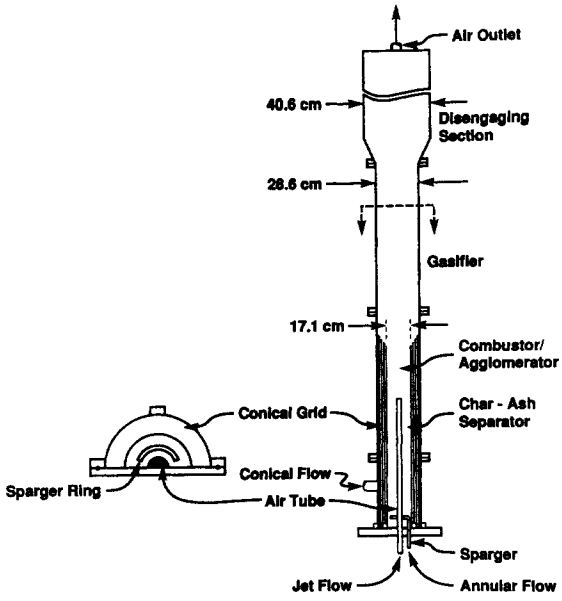

Figure 1. Westinghouse 30 cm dia. cold flow rig.
Yang and Keairns (1978)

Table 1 summarizes the solid and gas properties, and a specific set of flow rates from the Westinghouse cold flow reactor.

The KRW cold flow experimental apparatus is also a semicircular design, with a transparent front face and small window ports on the curved backside for observing the fluidization. Total height of the rig is 914 cm, with an inside diameter of 300 cm. While there are several variations of the KRW geometry, only deep-bed, 10-inch nozzle experiments, and the operating conditions corresponding to set points 3 and 15 of the test series TP-M010-1, are considered in the present study. A diagram of the deep-bed, 10-inch nozzle configuration is shown in Figure 2. For the TP-M010-1 experiments, with crushed acrylic particles, Yang et al. (1984) calculate a weighted particle size of 1,416 μm. Tables 2 and 3 contain the flow rates for set points 3 and 15 from test series TP-M010-1, respectively, and also include important solid and gas properties of the KRW environment. It is noted that in Tables 2 and 3, as well as in Table 1, the flow rates are actual flows corresponding to the semicircular geometries and central injectors. The next section discusses how these physical conditions are applied to the CHEMFLUB axisymmetric finite-difference scheme.

Numerical construction of reactors using CHEMFLUB

The finite-difference character of the CHEMFLUB model provides the means for the numerical construction of any practical reactor geometry. Two different classes of calculations are

Table 1. Experimental Conditions, Westinghouse 30 cm dia. Cold Flow Rig

Particle dia., μm	2,800
Particle density, g/cm^3	0.21
Mass flow, air tube, g/s	13.7
Mass flow, annulus, g/s	5.38
Mass flow, conical grid, g/s	0.45
Reactor pressure, atm	1.0
Reactor temp., K	293

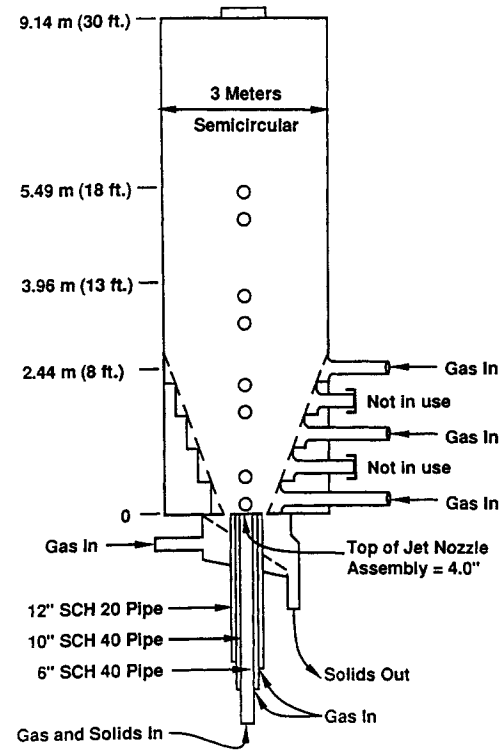

Figure 2. KRW 300 cm dia. deep bed cold flow rig.
Yang, et al. (1984)

presented herein. First, there are those for the basic configuration of each reactor, in which the axisymmetric finite-difference grid is organized to represent the actual rig geometry. Second, in the case of the Westinghouse rig a uniform porous plate injector configuration is introduced. In that configuration a uniform flow through a plate replaces the actual injector, and a simple cylinder replaces the actual rig. This calculation is used to determine the effects of reactor wall boundary conditions and uniform flow distribution on bubble formation. The Eulerian finite-difference grid and zones of gas input for these different geometries are shown in Figures 3–5.

Figure 3 illustrates the basic Westinghouse 30 cm dia. cold flow geometry. The centerline of the reactor is on the left side of the figure, while the right side is the outer wall of the rig. Fifty

Table 2. Experimental Conditions, KRW 300 cm dia. Cold Flow Rig

Test Series TP-M010-1, Set Point 3	
Particle dia., μm	1,416
Particle density, g/cm^3	1.19
Mass flow, air tube, g/s	17.7
Mass flow, annulus, g/s	11.2
Mass flow, shroud, g/s	4.4
Mass flow, conical grid, g/s	
Chamber 1	14.3
Chamber 3	28.7
Chamber 5	51.5
Mass flow, solids transport, g/s	9.2
Solids feed	0.0
Superficial velocity, cm/s	62
Reactor pressure, atm	1.0
Reactor temp., K	293

Table 3. Experimental Conditions, KRW 300 cm dia. Cold Flow Rig

Test Series TP-M010-1, Set Point 15	
Particle dia., μm	1,416
Particle density, g/cm^3	1.19
Mass flow, air tube, g/s	68.2
Mass flow, annulus, g/s	11.1
Mass flow, shroud, g/s	4.4
Mass flow, conical grid, g/s	
Chamber 1	14.2
Chamber 3	28.6
Chamber 5	50.7
Mass flow, solids transport, g/s	9.3
Solids feed	0.0
Superficial velocity, cm/s	82
Reactor pressure, atm	1.0
Reactor temp., K	293

zones in the axial direction and eight zones in the radial direction are used to establish an axisymmetric analog of the Westinghouse 30 cm dia. cold flow rig. All zones are of equal size: 1.8 cm wide and 3.6 cm high. The crosshatched zones in Figure 3 denote the gas input zones, which simulate the air tube, annular, and conical grid flows. The first zone on the centerline corresponds to the air tube flow, with the annular flow in the next four zones. Finally, conical flow is supplied by the first zone along the conical grid.

The mass flow per unit area for the solids transport tube, air

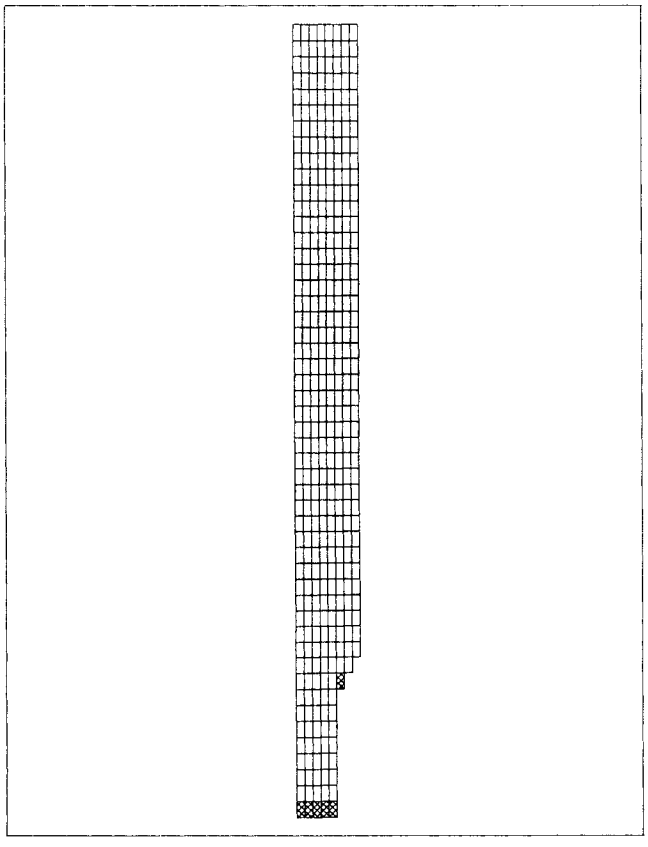

Figure 3. CHEMFLUB axisymmetric finite-difference construction of Westinghouse 30 cm dia. cold flow rig.
Axis of symmetry on left

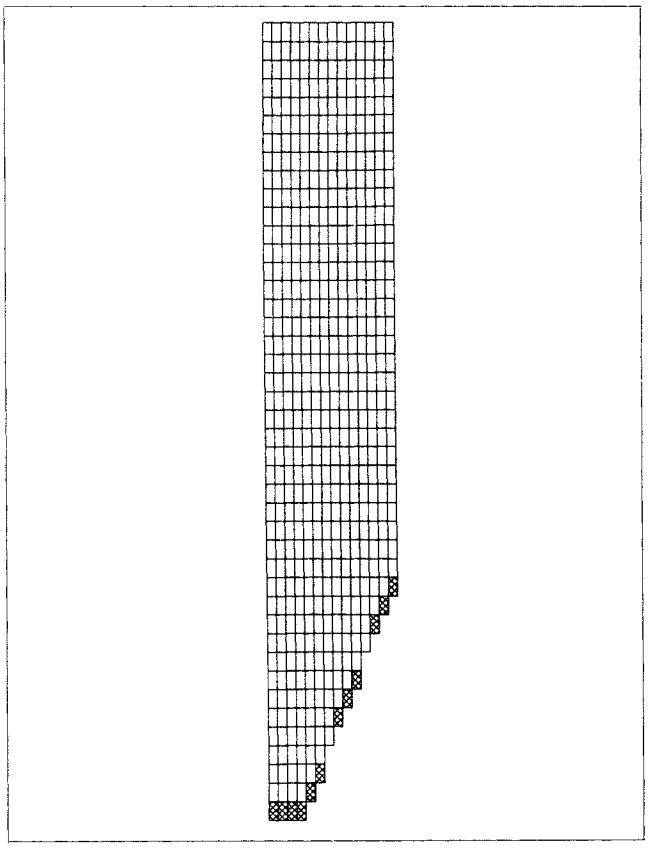

Figure 4. CHEMFLUB axisymmetric finite-difference construction of KRW 300 cm dia. cold flow rig.
Axis of symmetry on left.

tube, annulus, and conical grid, is observed in accordance with the experimental conditions. These mass flows are divided up into the gas input zones of the appropriate region so that the mass flow per unit area is a constant. This means that the total mass flow for each of the regions in the full axisymmetric calculations are twice the values reported in Tables 1–3 for the semicircular cold flow rigs. It is noted that using the gas mass flow, rather than the gas velocity, to define the respective gas input zones is consistent with the neglect of the gas inertia in the CHEMFLUB model.

The KRW 300 cm dia. cold flow geometry and gas input zones used in CHEMFLUB are displayed in Figure 4. Here solids transport tube, air tube, and shroud gas flow are all concentrated in the first crosshatched zone, on the left. In the set point 3 and 15, TP-M010-1 experiments there is no solids feed through the solids transport tube, only gas flow. Annular flow enters through the next three zones and conical grid flow is divided into the three remaining regions of gas input zones. The distribution of flow in the KRW calculations is determined using the same procedure, described above, for the Westinghouse calculations.

Finally, the initial condition in all of the CHEMFLUB calculations is that of particles and gas at rest.

Numerical Predictions for Axisymmetric Models of Westinghouse and KRW Cold Flow Rigs

CHEMFLUB yields a representation of the particle and gas flows in the fluidized bed through the calculation of an initial-

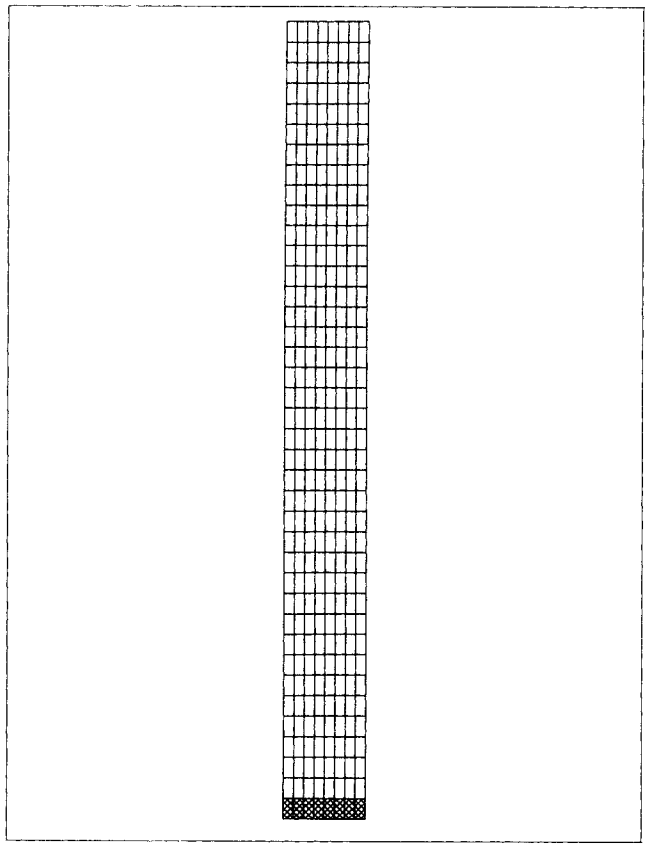

Figure 5. CHEMFLUB axisymmetric finite-difference construction of Westinghouse uniform porous plate injector geometry.
Axis of symmetry on left

boundary value problem. That calculation, as is also true for the actual fluidized bed, never attains a steady flow condition, except in the limiting case of minimum fluidization.

While all of the dependent variables in the basic Eqs. 1–5 are computed as a function of time and spatial location in the axisymmetric geometry of the rigs, only the particle positions will be displayed herein. These aggregate particle histories show the evolution of the jets occurring at the injector(s) and the development and rise of bubbles through the rigs. The experiments of Yang and Keairns (1978) and Yang et al. (1984) yield substantial data on jets and bubbles and consequently those aspects of the CHEMFLUB predictions are emphasized herein. Indeed, it might be said that the predicted particle positions provide a numerical experiment which arises from the finite-difference solution of Eqs. 1–5 and the associated boundary and initial conditions. The validity of the model is assessed through quantitative comparison with the actual experiments.

Results: Westinghouse 30 cm dia. cold flow rig

The prediction of a time sequence of jet penetration and bubble motion for the Westinghouse 30 cm dia. cold flow rig is shown in Figure 6. The initial and boundary conditions for that calculation are specified in Table 1 and Figure 3, where the central air tube is at the base of the reactor. A nonslip boundary condition on particle motion is prescribed at the outer wall. The particle shape factor is 0.8. Each frame in the sequence shows

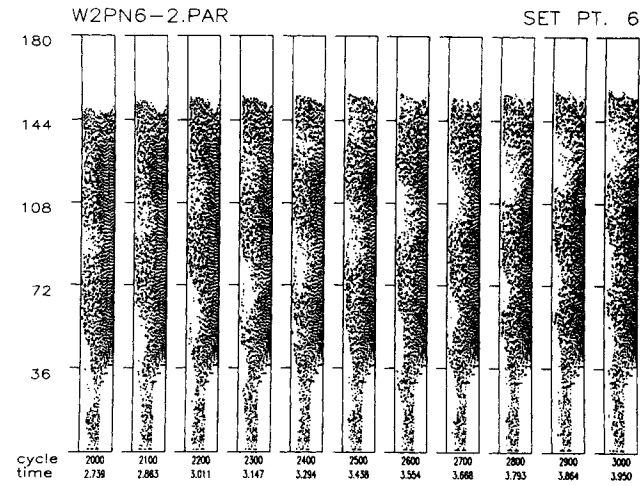

Figure 6. CHEMFLUB prediction of hydrodynamic mixing in axisymmetric Westinghouse 300 cm dia. cold flow rig.
Each frame in the time sequence shows axisymmetric geometry, with rig centerline on the left, outer radius on the right. Dimensions in cm, time in s

the axisymmetric geometry, where again, the centerline of the reactor is on the left side of each frame and the outer radius of the reactor is on the right side. The representative particles are indicated by the black dots. Voids such as jets and bubbles remain white. The dimensions along the lefthand side of the figure indicate height in cm. The time at the bottom is in seconds. It is noted that there is broad general agreement between Figure 6 and previous CHEMFLUB numerical calculations presented by Blake and Chen (1981). The calculations of Blake and Chen use a shape factor of 1.0, and the original algorithms in CHEMFLUB (Chen, 1981). This apparent insensitivity to shape factor and the modified algorithms in the present study is likely a consequence of rig geometry, flow regime, and particle size.

From the time sequence in Figure 6, jet and bubble dimensions and time histories can be calculated and compared to experimental observations. The predicted boundaries of the jet and the bubble correspond to the abrupt transition between a void and a particle-loaded regime. For example, jet penetration height, defined at detachment of the bubble from the jet, is observed to be approximately 58 cm. This value is consistent with the data of Yang and Keairns (1978), which for similar superficial velocities, indicate a range of values between 58 and 67 cm.

Figure 7 presents a comparison of computer simulation and experimental observations of jet penetration within a nondimensional format. The figure is based upon a correlation developed by Blake et al. (1990), in which the jet penetration height, l, is nondimensionalized by d_o, the diameter of the injector. The ordinate is the experimental observation, while the abscissa is the theoretical value, obtained from the correlation. The correlation was developed utilizing the data points shown in the figure. Among those points are data taken from experiments conducted in the Westinghouse and KRW experimental rigs. Most of the data points are bounded by lines that represent a 40% variation from the correlation. The Westinghouse experimental data are represented by the + symbol. CHEMFLUB's calculation of l/d_o is in good agreement with the Westinghouse data

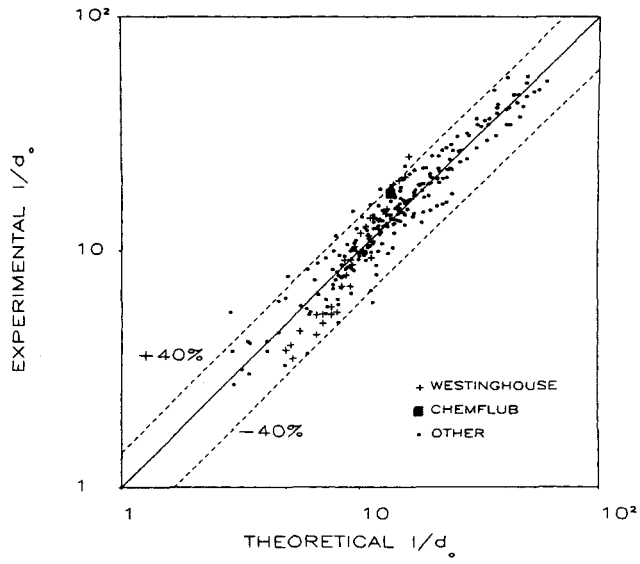

Figure 7. CHEMFLUB Westinghouse calculation of jet penetration height, data, and correlation of Blake et al. (1990).

Experimental data plotted as ordinate, corresponding CHEMFLUB prediction or correlation plotted as abcissa.

$$\frac{l}{d_o} = 26.9\left(\frac{v^2}{gd_o}\right)^{0.322}\left(\frac{\rho}{\rho^s}\right)^{0.325}\left(\frac{\rho^s v d^2}{\mu d_o}\right)^{-0.124}$$

and the correlation. Therefore, the correlation provides a validation of the CHEMFLUB prediction.

The characteristics of the hydrodynamic mixing, including jet penetration, obtained from the CHEMFLUB calculation in Figure 6, are presented in Table 4.

The CHEMFLUB Westinghouse simulation results can also be compared with the theory of Blake and Webber (1987), relating normalized bubble velocity and bubble dimensions. The data of Rowe and Partridge (1965) and of Park et al. (1969) are shown, together with the theory and the CHEMFLUB prediction, in Figure 8. The bubble velocity, V_{bubble}, is normalized by $(gd_{bed})^{1/2}$, where d_{bed} is the diameter of the reactor. The bubble dimension is in the form $(d_{bubble}/d_{bed})^{1/2}$, with d_{bubble} being the effective diameter of the bubble in the experiments and the axial length of the bubble in Blake and Webber's theory. That theory predicts bubble velocity for the range of bubble sizes between the limits of isolated bubbles and slugs; these limits define an envelope bounded by the upper and lower curves, respectively, in Figure 8. In this comparison of the numerical calculation and experimental observation, CHEMFLUB is within the scatter of the data and is well within the envelope. It is noted that the theory is for a single gas bubble injected into a bed at minimum

Table 4. CHEMFLUB Predictions for Westinghouse 30 cm dia. Cold Flow Rig

	CHEMFLUB	Exp.
Bubble radial dimension, cm	15	—
Bubble axial dimension, cm	29	—
Bubble velocity, cm/s	75	—
Bubble frequency, rate/min	42	—
Jet penetration, cm	58	58–67
Jet frequency, rate/min	115	—

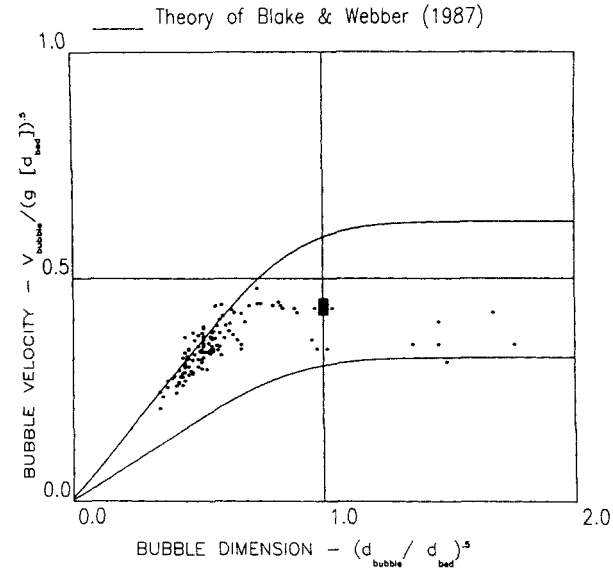

Figure 8. CHEMFLUB Westinghouse calculation of bubble velocity, data, and theory of Blake and Webber (1987).

● Park et al. (1969), Rowe and Partridge (1965).
■ CHEMFLUB Westinghouse calculation

fluidization. It is believed that the bubble velocities of the CHEMFLUB calculation reflect the superficial velocities produced by the air tube and annulus flows, whereby the rise velocity of the bubble is enhanced (Davidson et al. 1977).

Results: Westinghouse uniform porous plate injector calculations

The calculation of fluidization in the uniform porous plate injector geometry of Figure 5 can be used to assess the role of the central jet on bubble formation in the basic geometry of Figure 3. Again, the porous plate replaces the solids transport tube, air tube, annulus, and conical grid in the basic geometry, but the same superficial velocity or total mass flow is used in both configurations (Table 1). Also, two different calculations are performed, corresponding to two different boundary conditions on solid velocity at the wall of the reactor. In one calculation the particles have zero tangential velocity at the wall (nonslip), while in the other the particle slips with respect to the wall. This is done to assess the influence of the wall in the initiation of bubbles.

For this case of the uniform porous plate injector, some interesting predictions arise. The bubble formation is shown in Figures 9 and 10 for, respectively, the slip and nonslip boundary conditions. It is observed that even with slip at the wall there is preferential gas flow up the center of the Westinghouse rig. The predicted time sequences in Figures 9 and 10 are very similar. Also, relative to the calculation for the basic Westinghouse rig in Figure 6, bubbles predicted in the uniform porous plate injector rig are qualitatively similar. For example, in both Figure 6 and Figure 10 the bubbles develop and rise in the center of the rig, and solids flow down along the outer circumference; however in Figure 10 the bubbles are smaller and more dispersed.

The conclusion is that in the Westinghouse 30 cm dia. geometry, the nature and size of the bubble is influenced by central jet flow, but that total mass flow in the Westinghouse environment appears to dominate bubble formation.

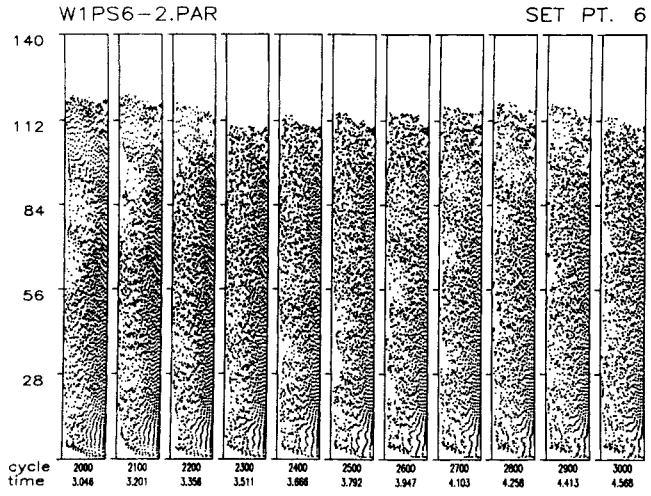

Figure 9. CHEMFLUB prediction of bubble motion in Westinghouse uniform porous plate injector configuration with slip boundary.

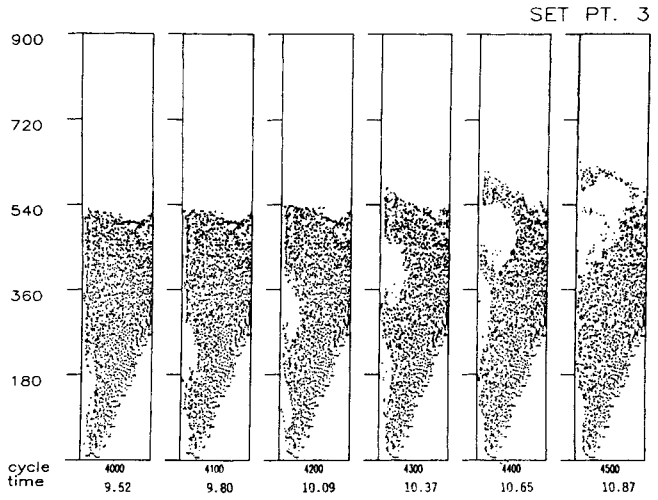

Figure 11. CHEMFLUB prediction of hydrodynamic mixing in axisymmetric KRW 300 cm dia. cold flow rig.

Each frame in the time sequence shows axisymmetric geometry, with rig centerline on the left, outer radius on the right. Dimensions in cm, time in s.

Results: KRW 300 cm dia. cold flow rig

The prediction of a time sequence of jet penetration and bubble motion for the KRW 300 cm dia. cold flow rig is shown in Figure 11. The initial and boundary conditions for that calculation are specified in Table 2 and Figure 4, together with a slip boundary condition on particle motion at the outer wall. The particle shape factor is 0.8. Table 5 presents a summary of the hydrodynamic predictions in Figure 11, together with the experimental observations from Yang et al. (1984). The experimental measurements are from TP-M010-1 set point 3, except for those of bubble axial dimension and jet frequency. However, the latter data are chosen from analogous runs reported by Yang et al. Most of the CHEMFLUB predictions are within the standard deviation of the averaged experimental observations. In Figure 12 the prediction of bubble velocity is compared with KRW data from TP-M010-1, the theory of Blake and Webber (1987), and other data on bubble velocity. The CHEMFLUB prediction is within the scatter of the KRW data, although it is perhaps high for the size of the bubble.

In Figure 13, l/d_o from the CHEMFLUB calculation is compared with the KRW data, represented by the + symbol, and the correlation of Blake et al. The CHEMFLUB calculation is consistent with the KRW data and well within the bounds of the correlation, indicating agreement between the numerical prediction and experimental observations.

From Table 5 it is observed that the CHEMFLUB prediction of characteristic bubble frequency is within 10% of the experimental observations. Characteristic frequencies are also measured in the vicinity of the injector. For example, the TP-M016-2 experiments indicate characteristic frequencies between 117 and 135 per min. From the calculation in Figure 11 the CHEMFLUB prediction is 90 per min (Table 5). It is possible that some experimental discrepancies exist in the interpretation of jet frequency. However, the likely source of the difference between the calculation and the experiment is the dispersion that is caused by the finite-difference technique and which produces a damping of the high-frequency signals. Alternatively, the neglect of the gas inertia in the momentum equations of the model may contribute to this damping.

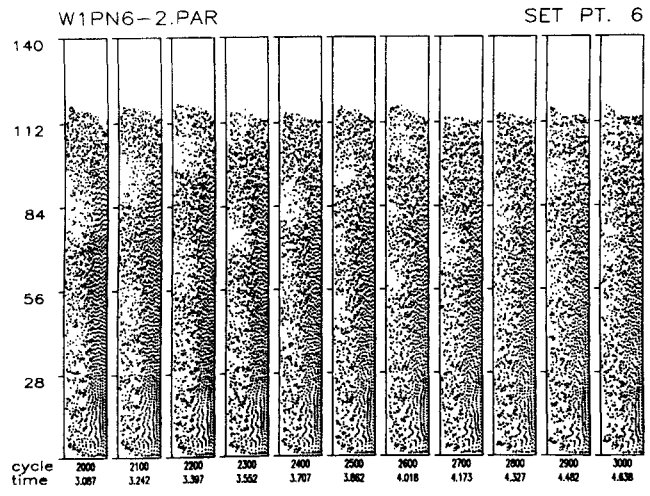

Figure 10. CHEMFLUB prediction of bubble motion in Westinghouse uniform porous plate injector configuration with nonslip boundary.

Conclusions

A shape factor is added to the particle-gas drag relationship in the CHEMFLUB model and some algorithms are modified to

Table 5. CHEMFLUB Predictions for KRW 300 cm dia. Cold Flow Rig

	CHEMFLUB	Exp.
Bubble radial dimension, cm	96	94 ± 25
Bubble axial dimension, cm	130	143–192*
Bubble velocity, cm/s	310	185 ± 72
Bubble frequency, rate/min	30	33
Jet penetration, cm	180	160 ± 19
Jet frequency, rate/min	90	117–135*

*Indirect comparisons, see text

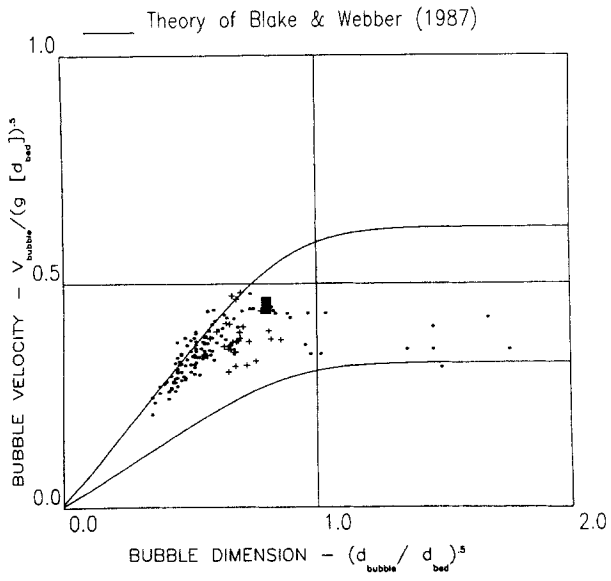

Figure 12. CHEMFLUB KRW calculation of bubble velocity data, and theory of Blake and Webber (1987).

● Park et al. (1969), Rowe and Partridge (1965)
■ CHEMFLUB KRW calculation
+ KRW data, Yang et al. (1984)

improve the numerical formulation. The modified CHEMFLUB predicts fluidized bed hydrodynamics that are consistent with earlier results of Blake and Chen (1981) for the Westinghouse rig, and that are in agreement with experimental observations. Further, when the model is applied to the KRW rig a good comparison between the calculations and many

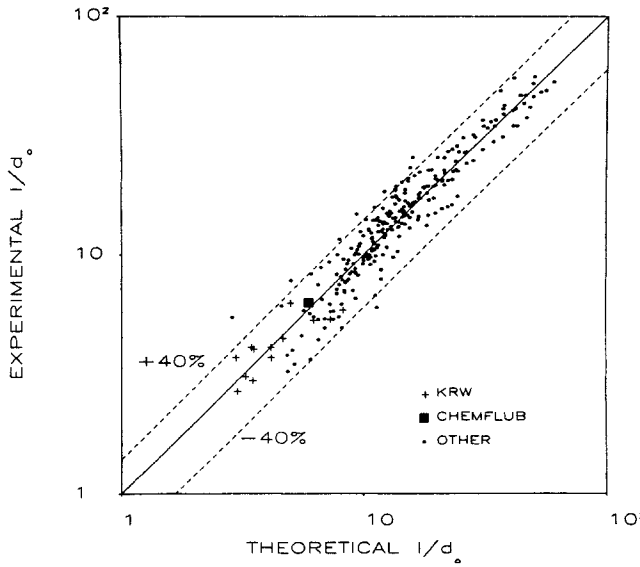

Figure 13. CHEMFLUB KRW calculation of jet penetration height, data, and correlation of Blake et al. (1990).

Experimental data plotted as ordinate, corresponding CHEMFLUB prediction or correlation plotted as abcissa

$$\frac{l}{d_o} = 26.9\left(\frac{v^2}{gd_o}\right)^{0.322}\left(\frac{\rho}{\rho^s}\right)^{0.325}\left(\frac{\rho^s v d^2}{\mu d_o}\right)^{-0.124}$$

aspects of the experimental observations are demonstrated. However, some differences between calculation and experiment are observed.

A summary of the comparisons between the CHEMFLUB predictions and the experimental observations is:

- Jet penetration. CHEMFLUB provides predictions of jet penetration height that are in agreement with the Westinghouse and KRW experiments and with existing correlations.
- Bubble velocity. CHEMFLUB yields bubble velocities that are, in general, higher than specific KRW experiments, but are within the bounds of data and are consistent with existing correlations.
- Bubble frequency. Bubble frequencies produced by CHEMFLUB are within 10% of the KRW experimental observations.
- Bubble geometry. CHEMFLUB predicts bubbles that are equal to the size of those observed in the KRW experiments but are more oblong in shape.
- Jet frequency. High characteristic frequencies observed near the jet nozzle of the KRW rig are not accurately predicted by CHEMFLUB.

Also, the CHEMFLUB model is used to investigate bubbles that are produced in the Westinghouse rig when the central injector and the conical base is replaced by a uniform porous plate injector. These calculations, in a limited fashion, permit an assessment of the role of the central injector in bubble formation. With the porous plate and with superficial velocities comparable to those in the basic Westinghouse geometry, bubbles occur and rise along the centerline of the rig. However, those bubbles are smaller and more dispersed than those in the basic Westinghouse geometry.

Naturally, the results of this and any similar computational study are limited by the physicochemical assumptions in the model, the resolution of the finite-difference computational zones, and the scope and number of the calculations. For example, in the CHEMFLUB simulation of the uniform porous plate injector rig, the dispersion of the bubbles may be affected by the size of those bubbles relative to the size of the computational zones.

The demonstrated agreement between the CHEMFLUB predictions and the experimental data provides a partial validation of the assumptions in the model regarding particle-particle and particle-gas forces. However, some of the discrepancies in the comparison suggest the need for more sophisticated representations of such forces. For example, at higher flow rates corresponding to the maximum superficial velocities in the KRW experiments, it is noted, without proof, that CHEMFLUB predicts bubbling and elutriation in excess of that observed in the experiments. It is believed that this divergence of CHEMFLUB and the experiments is related to the particle-particle forces or solid phase rheology in the model. Recent work on granular stress models (Lun et al., 1984) suggests that a more complicated formulation is both practical and advantageous. Also, there are alternative numerical algorithms (Gidaspow and Ettehadieh, 1983; Gidaspow, 1986) which may be more open than CHEMFLUB to the incorporation of such constitutive equations and, for example, multiple particle sizes (Syamlal and O'Brien, 1988).

Acknowledgment

This research is sponsored, in part, by USDOE Contract DE-AC21-85MC22062 to the Department of Mechanical Engineering at the Uni-

versity of Massachusetts, Amherst. The authors appreciate the support and encouragement of L. Jarr and H. F. Bauer of the USDOE Morgantown Energy Technology Center. W. C. Yang of the Westinghouse Corporate Research and Development Center provided data and interpretation of the experimental environments of the Westinghouse and KRW cold flow rigs.

Notation

$\tilde{A}$ = specific surface area of particle
B = particle-gas drag coefficient
d = particle diameter
d_o = injector diameter
d_{bed} = bed diameter
d_{bubble} = bubble diameter
F_1, F_2 = empirical functions in permeability relationship
K = permeability
l = jet penetration height
N = modified Reynolds number in permeability relationship
p = gas pressure
p^s = solid pressure
t = time
u_i = solid velocity vector
v = gas velocity
v_{bubble} = bubble velocity
v_i = gas velocity vector
x_i = Cartesian coordinate

Greek letters

δ_{ij} = Kronecker delta
θ = solidity or solid volume fraction
λ^s, μ^s = solid viscosities
μ = gas viscosity
ρ = gas density
ρ^s = solid (grain) density
τ_{ij} = solid stress tensor
ϕ_s = shape factor

Literature Cited

Anderson, T. B., and R. Jackson, "Fluid Mechanical Description of Fluidized Beds, Equations of Motion," *Ind. Eng. Chem. Fundam.*, **6,** 527 (1967).

Blake, T. R., and P. J. Chen, "Computer Modeling of Fluidized Bed Coal Gasification Reactors," *Am. Chem. Soc. Symp. Ser.*, **168,** 8 (1981).

Blake, T. R., and M. R. Webber, "A Theoretical Representation of Single Bubble Motion in a Cylindrical Gas Fluidized Bed," *Chem. Eng. Sci.*, **42,** 2687 (1987).

Blake, T. R., H. A. Webb, and P. B. Sunderland, "The Nondimensionalization of Equations Describing Fluidization with Application to the Correlation of Jet Penetration Height," *Chem. Eng. Sci.*, **45,** 365 (1990).

Chan, R. K.-C., M. J. Chiou, D. E. Dietrich, D. R. Dion, H. H. Klein, D. H. Kaird, H. B. Levine, C. A. Meister, M. F. Scharff, and B. Srinivas, "Computer Modeling of Mixing and Agglomeration in Coal Conversion Reactors. I," U.S. DOE Report DOE/ET/10329-1211, vol. I (1982).

Chen, P. J., "Computer Modeling of Coal Gasification Reactors," U.S. DOE Report DOE/ET/1042-T1, vol. III (1981).

Davidson, J. R., and D. Harrison, *Fluidized Particles*, Cambridge Univ. Press (1963).

Davidson, J. R., D. Harrison, R. C. Darton, and R. D. LaNanze, "Two-phase Theory of Fluidization and Its Application to Chemical Reactors," *Chemical Reactor Theory*, L. Lapidus and N. R. Amundson, eds., Prentice-Hall, Englewood Cliffs, NJ 583 (1977).

Fitzgerald, T. J., and L. R. Glicksman, "Testing of Cold Scaled Bed Modeling for Fluidized Bed Combustors," 75th Ann. AIChE Meet., Washington, DC (1983).

Gidaspow, D., "Hydrodynamics of Fluidization and Heat Transfer: Supercomputer Applications," *Appl. Mech. Rev.*, **39,** 1 (1986).

Gidaspow, D., and B. Ettehadieh, "Fluidization in a Two-dimensional Bed with a Jet. 2: Hydrodynamic Modeling," *Ind. Eng. Chem. Fundam.*, **22,** 193 (1983).

Gidaspow, D., B. Ettehadieh, and R. W. Lyczkowski, "Computer Modeling of Sand in a Two-dimensional Bed with a Jet," Paper 63a, AIChE Ann. Meet., New Orleans (1981).

Glicksman, L. R., "Scaling Relationships for Fluidized Beds," *Chem. Eng. Sci.*, **39,** 1373 (1984).

———, "Scaling Relationships for Fluidized Beds," *Chem. Eng. Sci.*, **43,** 1419 (1988).

Kunii, D., and O. Levenspiel, *Fluidization Engineering*, Wiley, New York (1969).

Lun, C. K. K., S. B. Savage, D. J. Jeffrey, and N. Chepurnity, "Kinetic Theories for Granular Flow: Inelastic Particles in Couette Flow and Slightly Inelastic Particles in a General Flow," *J. Fluid Mech.*, **140,** 223 (1984).

Park, W. H., W. K. Kang, C. E. Capes, and G. L. Oseberg, "The Properties of Bubbles in Fluidized Beds of Conducting Particles as Measured by an Electroresistivity Probe," *Chem. Eng. Sci.*, **24,** 851 (1969).

Pritchett, J. W., T. R. Blake, and S. K. Garg, "A Numerical Model of Gas Fluidized Beds," *AIChE Symp. Ser.*, **74** (176), 134 (1978).

Rowe, P. N. and B. A. Partridge, "An X-ray Study of Bubbles in Fluidized Beds," *Trans. Inst. Chem. Engrs.*, **43,** T157 (1965).

Schneyer, G. P., E. W. Peterson, P. J. Chen, J. L. Cook, D. H. Brownell, Jr., and T. R. Blake, "Computer Modeling of Coal Gasification Reactors," U.S. DOE Report DOE/ET/1042-T1, vols. I, II (1981).

Syamlal, M., and T. J. O'Brien, "Simulation of Granular Layer Inversion in Liquid Fluidized Beds," *Int. J. Multiph. Flow*, **14,** 473 (1988).

Yang, W. C., B. Ettehadieh, T. C. Anestis, R. E. Gizzie, and G. B. Haldipur, "Advanced Development of a Pressurized Ash Agglomerating Fluidized-bed Coal Gasification System," Topical Report, U.S. DOE Report FE-19122-46, vols. I, II (1984).

Yang, W. C., and D. L. Keairns, "Design and Operating Parameters for a Fluidized Bed Agglomerating Combuster/Gasifier," *Fluidization*, J. F. Davidson and D. L. Keairns, eds., Cambridge Univ. Press, 208 (1978).

Yates, J. G., *Fundamentals of Fluidized-bed Chemical Processes*, Butterworth (1983).

Manuscript received July 31, 1989, and revision received Dec. 20, 1989.

See NAPS document no. 04744 for 19 pages of supplementary material. Order from NAPS c/o Microfiche Publications, P.O. Box 3513, Grand Central Station, New York, NY 10163. Remit in advance in U.S. funds only $7.75 for photocopies or $4.00 for microfiche. Outside the U.S. and Canada, add postage of $4.50 for the first 20 pages and $1.00 for each of 10 pages of material thereafter, $1.50 for microfiche postage.